



# Anomalous steady-state and spatio-temporal features of methane oxidation on Pt/Pd/Al<sub>2</sub>O<sub>3</sub> monolith spanning lean and rich conditions

Gregory S. Bugosh<sup>a</sup>, Vencon G. Easterling<sup>a</sup>, Irene A. Rusakova<sup>b</sup>, Michael P. Harold<sup>a,\*</sup>

<sup>a</sup> Texas Center for Clean Engines, Emissions & Fuels, Department of Chemical and Biomolecular Engineering, University of Houston, Houston, TX 77204, USA

<sup>b</sup> Texas Center for Superconductivity, Department of Physics, University of Houston, Houston, TX 77204, USA

## ARTICLE INFO

### Article history:

Received 25 June 2014

Received in revised form

22 September 2014

Accepted 24 September 2014

Available online 2 October 2014

### Keywords:

Methane oxidation

Platinum

Palladium

Hysteresis

SpaciMS.

## ABSTRACT

The steady-state and transient features of methane oxidation on a Pt/Pd/Al<sub>2</sub>O<sub>3</sub> washcoated monolith are reported for a wide range of temperatures and feed gas compositions. Above 400 °C the methane conversion dependence on the O<sub>2</sub> feed concentration exhibits a multiplicity of states. With increasing temperature the multiplicity, in the form of a clockwise hysteresis in the rich regime, expands over a broader O<sub>2</sub> concentration range. At the highest temperature considered (538 °C) extinction occurs near the rich-lean transition (O<sub>2</sub>/CH<sub>4</sub> = 1.9), while ignition occurs at O<sub>2</sub>/CH<sub>4</sub> ~ 0.6. A low conversion state exists for all O<sub>2</sub> concentrations exceeding the ignition concentration at this temperature. In the rich regime, multiple high conversion states are encountered, all of which produce a mixture of CO, CO<sub>2</sub>, H<sub>2</sub>, and H<sub>2</sub>O. Only the lowest conversion branch of this group is a steady-state. Another high conversion branch is encountered for O<sub>2</sub> concentrations spanning a wide lean regime (2 < O<sub>2</sub>/CH<sub>4</sub> < 125). Spatially resolved capillary-inlet mass spectrometry (SpaciMS) measurements reveal two primary zones within the monolith. In the front zone, complete oxidation of methane to CO<sub>2</sub> is dominant until the O<sub>2</sub> concentration decreases downstream below a critical value. Beyond that point both CO and H<sub>2</sub> are produced, revealing the emergence of methane partial oxidation, steam reforming, and water gas shift (WGS) reactions. Transmission electron microscopy and energy dispersive spectroscopy reveal particles having a distribution of sizes and compositions, Pt/Pd ratios ranging from 10 (Pt-rich) to 0.2 (Pd-rich), and particles having an average size of ~15–20 nm. Accordingly, the conversion trends and spatiotemporal data are interpreted with a mechanistic model accounting for contributions by Pt, Pd, and PdO phases. For example, methane conversion in the lean regime is likely dominated by an active PdO phase, while the rich oxidation behavior is strongly affected by the oxygen self-poisoning on metallic Pd and Pt sites. The low conversion branch is attributed to inhibition by O<sub>2</sub> adsorption occupying the metallic catalyst sites, although the state is unstable in the lean regime as the more active PdO phase forms. The multiple high conversion state branches in the rich regime and the associated slow transient approach to a single stable high conversion branch are attributed to the supply of oxygen from the underlying bulk of PdO which favors methane partial oxidation.

© 2014 Elsevier B.V. All rights reserved.

## 1. Introduction

Advances in hydraulic fracturing technology have led to low-price domestic natural gas, increasing the economic incentive for natural gas powered engines [1]. As a result, the use of natural gas (NG) as a transportation fuel in the liquefied (LNG) and compressed (CNG) forms is expected to grow. LNG and CNG vehicles generally have lower emissions of particulate matter (PM), SO<sub>x</sub>, and non-methane hydrocarbons (NMHC). On the other hand, methane emissions from NG-powered vehicles are much higher

than gasoline- and diesel-fueled vehicles. Historically, vehicular emission regulations have excluded methane from the HC limits, instead placing restrictions on NMHCs or non-methane organic gases (NMOG). While methane does not contribute to ozone formation, it is a potent greenhouse gas with a global warming potential more than 20 times that of CO<sub>2</sub> [2]. A consequence of this fact is the expected emergence of more stringent methane emission regulations in the coming years. For this reason there is a renewed interest in the development of improved catalytic converters for NG-powered vehicles.

While most hydrocarbons (HCs) and carbon monoxide (CO) emitted from internal combustion engines are readily abated by noble metal (Pt, Pd) catalyzed oxidation, CH<sub>4</sub> is notoriously

\* Corresponding author.

E-mail address: [mharold@uh.edu](mailto:mharold@uh.edu) (M.P. Harold).

non-reactive [3,4]. Stoichiometric (spark-ignited) NG-powered combustion engines have a comparatively low exhaust concentration of  $O_2$  (< 2%), so the three-way catalyst (TWC) is effective in simultaneously oxidizing CO and NMHC's and in reducing  $NO_x$ . The much less reactive methane passes through a monolith comprising  $Pt/Al_2O_3$  with little conversion at relevant space velocities ( $>10\text{ km h}^{-1}$ ) and temperatures below  $400^\circ\text{C}$  [5]. In contrast, lean-burn NG vehicles generally utilize Pd-based catalysts, and the large excess of oxygen in the exhaust readily forms palladium oxide (PdO), which is quite active for methane oxidation [6,7]. However, temperature excursions that may occur are problematic since PdO decomposes at temperatures exceeding  $\sim 600^\circ\text{C}$  even under oxidizing conditions [8,9]. This can lead to a decrease in conversion due to the lower activity of metallic Pd. Indeed, the dynamics of the PdO/Pd interconversion can result in variations in the methane conversion with time-on-stream [10–14]. For example, it was reported that for Pd catalysts the  $CH_4$  conversion depends on the direction of the change in feed composition [15,16]. The transient behavior is exacerbated by catalyst deactivation primarily through Pd crystallite agglomeration at high temperature. The addition of Pt to Pd/PdO has been reported to inhibit this sintering [17]. Recent work has shown that bimetallic Pt–Pd catalyst formulations have improved thermal stability compared to Pt- or Pd-only catalysts [18]. Further, the emergence of “dual fuel” CNG + diesel powered engines means that Pt/Pd catalysts will be used for methane oxidation since this is the common composition of diesel oxidation catalysts (DOCs). For these reasons, Pt/Pd formulations are interesting catalyst candidates for methane oxidation in the exhaust of lean-burn vehicles.

It is instructive to provide a mini-review of the extensive literature for the catalytic oxidation of methane on Pt, Pd, and Pt/Pd catalysts. Earlier fundamental research carried out of methane oxidation on Pt and Pd catalysts reveals several notable features. Gelin and Primet [4] reviewed the complete oxidation of methane on noble metal catalysts. In general, Pt is the more active catalyst under rich conditions, whereas Pd is the more active catalyst under lean conditions [15,19]. The reason for the latter is the formation of PdO, the more active form. In comparison, Pt oxide ( $PtO_2$ ) is unstable above  $400^\circ\text{C}$ , which is the minimal temperature needed to achieve a non-negligible conversion of methane at relevant space velocities. That said, Pt is more likely to exist in metallic form. On Pt and Pd catalysts exposed to rich conditions methane is converted to partially oxidized products CO and  $H_2$  in addition to  $CO_2$  and  $H_2O$ . Enhanced methane conversion at low oxygen feed concentration (fuel-rich) has previously been reported by Oh et al. [15], Subramanian et al. [20,21], and Lyubovsky et al. [22] over  $Al_2O_3$ -supported Pt and Pd. On Pt, methane oxidation exhibits a rate/conversion maximum with respect to  $O_2$  concentration [23,24]. The maximum demarcates a positive order regime ( $\sim 1$ ), in which the oxidation rate is limited by  $O_2$  adsorption, from a negative order regime ( $\sim -1$ ), in which the rate is inhibited by chemisorbed oxygen adatoms. The negative-order regime traverses the  $O_2/CH_4 = 2$  stoichiometric ratio. Under lean conditions Pd takes up much more than one monolayer of oxygen atoms. Corresponding to this uptake is an increase in the oxidation activity, clearly indicating that the existence of PdO, probably in a mixture with metallic Pd, is essential to provide activity. Under similar conditions on Pt, methane conversion is negligible due in part to the aforementioned instability of Pt oxide and site blocking by chemisorbed oxygen.

A deeper fundamental understanding of the mechanistic features of methane oxidation is emerging. Epling and Hoflund [25] showed that a mixture of Pd metal and PdO has a higher activity than Pd or PdO alone. They suggest that the Pd metal surface more easily dissociates the methane and that  $CH_x$  reaction intermediate surface species migrate to the PdO to be oxidized. Bell and coworkers [26,27] have advanced a similar mechanism: The dissociative chemisorption of methane is the rate-limiting step and

metallic Pd enhances its rate. The kinetics of lean methane oxidation on Pd at relevant temperatures ( $400$ – $800^\circ\text{C}$ ) show a first-order dependence on methane and zero-order dependence on  $O_2$  [28]. The first-order dependence is consistent with methane adsorption/activation being the rate-limiting step. Iglesia and coworkers presented detailed studies of the kinetics of methane oxidation on supported Pt and Pd clusters [24,29], complementing their earlier studies of methane oxidation by  $H_2O$  and  $CO_2$  [30]. Methane activation on Pd clusters is enhanced on a dual site comprising a vacant metal site ( $*$ ) and an O-occupied site ( $O-*$ ) [24]. This builds on a similar mechanism proposed by Fujimoto et al. [31] involving the dissociative oxidation of methane on adjacent Pd and PdO sites forming adsorbed  $CH_3$  and OH, respectively. A recent study by Zhang et al. [32] of methane oxidation on PdO using wire microcalorimetry supports these ideas. Chin and Iglesia [24] argued that  $CO_2$  and  $H_2O$  are the only products of oxidation at low conversion due in part to the much higher reactivity of CO with  $O-*$ . Methane oxidation on Pd clusters resulted in lower turnover frequencies because the stronger binding of O to high index planes of Pd means that the catalyst is less effective in activating methane. A number of investigators have shown the reversible nature of Pd oxidation by  $O_2$  and PdO reduction by  $H_2$  and  $CH_4$  [26,33–35]. This can lead to hysteresis behavior and long transients. Datye et al. [34] attributed the hysteresis in PdO reformation during a temperature decrease to inhibition by strongly bound oxygen on the Pd surface. A recent study by Amin et al. [36] shows interesting hysteresis effects for methane oxidation on a  $Pt/Al_2O_3$  monolith catalyst. Finally, a number of studies have reported that partial oxidation products  $H_2$  and CO are generated under  $O_2$  deficient conditions [37,38]. The aforementioned differences in reactivity of CO and  $CH_4$  suggest that the generation of  $H_2$  and CO follows a sequential mechanism in which  $CH_4$  and  $O_2$  react first to give  $CO_2$  and  $H_2O$ , and then  $CH_4$  reacts with  $H_2O$  to form CO and  $H_2$ , along with the water gas shift (WGS) reaction.

Recent studies of methane oxidation on combined Pt/Pd catalysts lend support to behavior reported on individual Pt, Pd, and PdO catalysts. This is due in part to the sustained existence of PdO as a separate phase in bi-metallic supported catalysts. The mixture of Pt and Pd is beneficial from both durability and activity standpoints. Narui et al. [17] showed that the addition of Pt to PdO inhibits deactivation through particle growth suppression with flattening of individual PdO crystallites. Ozawa et al. [39], using XRD analysis, showed that high temperature ( $750$ – $800^\circ\text{C}$ ) catalytic oxidation of methane resulted in less particle growth for a supported PdO catalyst containing a small amount of Pt compared to Pt-free PdO. Morlang et al. [40] examined bimetallic PtPd catalysts after thermal aging and found that PdO and Pt/Pd particles were both present. Further, they showed that the alloyed system resisted sintering. Persson et al. [41] carried out a systematic study of six catalysts for lean methane oxidation. They found that the most active and stable catalysts were  $Pd_{67}Pt_{33}$  and  $Pd_{50}Pt_{50}$ . Based on TEM imaging they concluded that PdO is present in close proximity to PtPd alloyed crystallites. Johns et al. [42] used a combination of spectroscopies to suggest that after high temperature calcination in air PdO is present as a separate phase in the presence of PtPd with no evidence of oxide formation on the PtPd metallic crystallites.

In this study we employ spatially resolved capillary-inlet mass spectrometry (SpaciMS) to follow the catalytic pathways of methane oxidation over a range of conditions. First developed by Partridge and coworkers [43,44] at Oak Ridge National Lab, SpaciMS has been shown to be a powerful tool for following catalytic reaction pathways by uncoupling the integral nature of monolith reactors. Choi et al. [45–48] studied  $NO_x$  storage and reduction using SpaciMS and determined the amount of catalyst required for storage varied based on sulfur exposure of the storage component and sintering of the precious metal components. Other studies

[49–52] have employed SpaciMS to decipher the integral production and consumption of species during the regeneration of lean NO<sub>x</sub> traps. Schmidt and coworkers [53] showed using SpaciMS that the oxidation and reforming zones depend on the precious metal identity (Pt, Pd, Rh).

Recently, measurements involving a spatio-temporal approach have investigated the effects of the capillary inside the channel of the monolith. In addition to their SpaciMS work [54–58], Epling et al. have used as well a Spaci-FTIR [59–61] in spatio-temporal measurements of various reaction systems. A study by the Deutschmann and coworkers has shown that capillary probe technique may introduce a systematic error due to flow restriction presented by the probe [62]. The restriction may result in a lower flow rate in the probe channel which would tend to lead to a higher conversion as a result of the longer contact time. The presence of the capillary restricts the flow rate in the channel containing the capillary which leads to an increase in flow in adjacent channels. This issue has been debated by Goguet and Partridge [63] who claim that Deutschmann's findings cannot be applied to different systems without considering the configuration and operating conditions. Deutschmann et al. have presented a response that systematically discusses the concerns proposed by Goguet et al. [64]. While this debate remains unresolved, we believe the SpaciMS technique provides a valuable *in situ* probe of the integral nature of reaction systems. However, some caution should be exercised in the application of quantitative SpaciMS data.

While a deeper understanding of methane oxidation on individual precious metal catalysts has emerged, studies of methane oxidation on combined Pt/Pd catalysts supported on monoliths have been comparatively sparse. To this end, in this study we investigate the oxidation of methane on a standard Pt/Pd monolithic catalyst. Wide ranges of O<sub>2</sub> feed concentrations and catalyst temperatures are investigated to map the methane conversion and product distribution. We determine the steady-state dependence, differentiate between steady-states and long transients, and identify transitions (bifurcations) between the different branches. SpaciMS measurements elucidate the interplay between chemical species as they react through the length of the monolith through key trends. Transmission electron microscopy (TEM) and energy dispersive spectroscopy (EDS) measurements provide insight about the size and composition of the metallic nanoparticles. Finally, a phenomenological model of the reaction system is described that is consistent with the measurements.

## 2. Experimental

The bench flow reactor setup (Fig. 1) includes mass flow controllers (MKS) for metering of cylinder-supplied gases (Praxair, Matheson), a quartz tube reactor within a tube furnace (Lindberg/Blue), and multiple thermocouples (Omega) for temperature monitoring and control. Heat tracing of post reactor lines minimized condensation. Gas composition analysis was accomplished by FTIR (Thermo Scientific Nicolet 6700) and mass spectrometer (Pfeiffer GSD 301). The FTIR was used to measure CH<sub>4</sub>, CO, and CO<sub>2</sub> concentrations in the bulk gas reactor effluent, as well as to confirm reactor feed concentrations through the use of a bypass line. The mass spectrometer capillary was connected by a computer-controlled stage (Zaber Technologies Inc.) for spatially resolved intra-channel measurements (SpaciMS). The fused silica capillary was inserted from the downstream end of the reactor (Fig. 1) and had inner and outer diameters of 150 and 363 μm, respectively. SpaciMS measurements were generally not taken at the very end of the monolith sample (2.5 cm) due to difficulty in reinserting the capillary into the channel. The gas concentration measurements enabled the closure of C, O, and H balances within ±10% during steady-state operation. Custom end pieces were fabricated to accommodate the thermocouple and SpaciMS capillary. Graphite/Vespel™ ferrules were utilized so that capillary measurements could be taken simultaneously with the FTIR effluent gas composition measurements.

The catalyst used in this study was a washcoated 400 cpsi cordierite monolith containing 60 g ft<sup>-3</sup> Pt/Pd in a 2:1 ratio by weight (~1:1 molar ratio) on γ-Al<sub>2</sub>O<sub>3</sub> support with a total wash-coat loading of 1.4 g in<sup>-3</sup> (0.085 g cm<sup>-3</sup>; supplied by BASF, Iselin, NJ). The sample core was cut to 1.27 cm diameter and 2.54 cm length using a diamond-tip cylindrical drill bit. Experiments were carried out using Ar as the diluent gas with a gas hourly space velocity (GHSV) of 60,000 h<sup>-1</sup> based on the overall monolith sample volume and standard conditions. Reported experimental temperatures were measured by a type K 0.51 mm o.d. thermocouple positioned 2 mm upstream of the front face of the catalyst. The typical methane concentration was 800 ppm while the O<sub>2</sub> was varied within the range of 100 ppm (0.01%) and 10% (by volume) with balance Ar. The stoichiometric number S<sub>N</sub> is used to characterize the oxidant/reductant ratio:

$$S_N = \frac{2C_{O_2}}{4C_{CH_4} + C_{CO}} \quad (1)$$

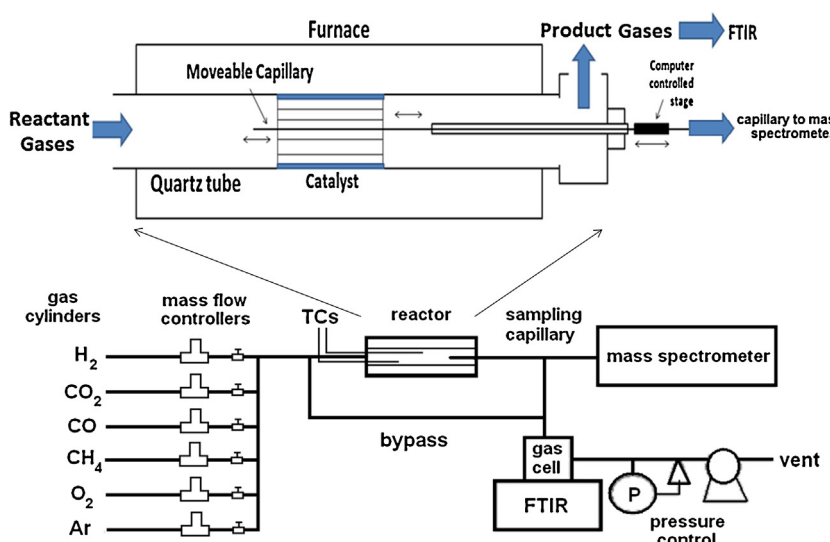


Fig. 1. Experiment setup and spatially resolved concentration measurement setup.

where  $C_i$  is the gas feed concentration of species  $i$ . Thus the gas mixture is lean if  $S_N > 1$ , stoichiometric if  $S_N = 1$ , and rich if  $S_N < 1$ . Finally, an estimate of the adiabatic temperature rise for the complete oxidation of 800 ppm CH<sub>4</sub> is  $\sim 30^\circ\text{C}$ , so the feed gas temperature was representative of the catalyst temperature.

Transmission electron microscopy (TEM) studies were performed at the Texas Center for Superconductivity at the University of Houston for catalyst characterization. The JEOL 2000FX and JEOL 2010 microscopes are equipped with energy dispersive spectrometers and were operated at 200 kV. Samples were prepared by removing some Pt/Pd/Al<sub>2</sub>O<sub>3</sub> washcoat from a relatively fresh-monolith sample, suspending the resulting powder in ethanol, and then ultrasonication and distributing the mixture onto a 300-mesh carbon-coated copper grid. Conventional and high resolution TEM imaging and EDS methods enabled the analysis of metal particle size and atomic composition.

### 3. Results

The dependence of the methane conversion on the O<sub>2</sub> feed concentration reveals complex behavior. In the experiment represented in Fig. 2a the O<sub>2</sub> feed concentration was varied over a wide range (0.01–10%) while the feed temperature was fixed at 538 °C and methane feed concentration fixed at 800 ppm. Fig. 2b shows an expansion of the low concentration range (O<sub>2</sub> concentration < 0.5%). At this methane concentration the O<sub>2</sub> concentration required for complete oxidation is 1600 ppm (0.16%); this corresponds to the  $S_N = 1$  value. The behavior in the rich ( $S_N < 1$ ) and lean regimes ( $S_N > 1$ ) are seen to be quite different. The data include a high conversion branch at high O<sub>2</sub> concentrations ( $S_N > 1$ ), a clockwise hysteresis loop at low concentrations ( $S_N < 1$ ), and a low conversion state that extends over nearly the entire O<sub>2</sub> concentration range (0.4 <  $S_N < 65$ ). Each of these is described in more detail next.

The lean oxidation resulted in a moderately high methane conversion (Fig. 2a). The data point at 10% O<sub>2</sub> and 73% conversion was obtained after ramping the feed temperature at a rate of 5 °C min<sup>-1</sup>

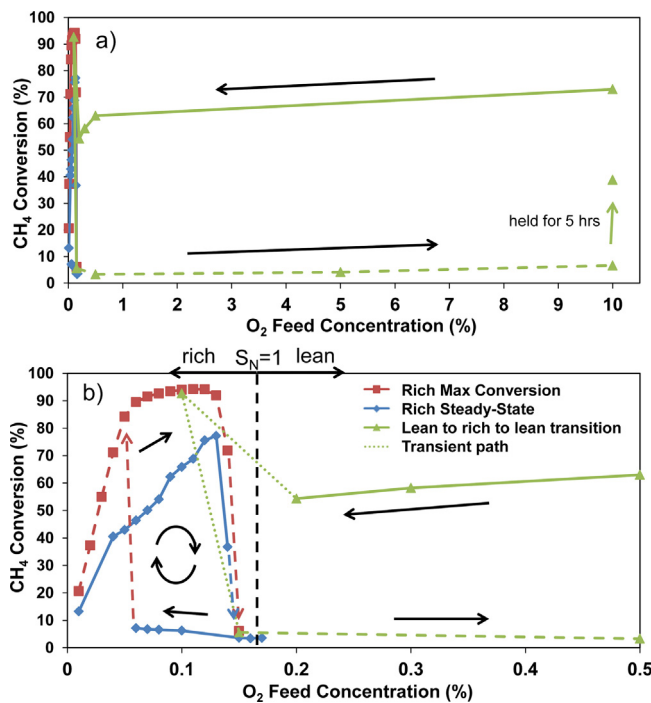


Fig. 2. Dependence of CH<sub>4</sub> conversion on O<sub>2</sub> feed concentration ( $T_f = 538^\circ\text{C}$ , 800 ppm CH<sub>4</sub>, GHSV = 60,000 h<sup>-1</sup>).

from 25 to 600 °C while the feed composition was held at 800 ppm CH<sub>4</sub> in 10% O<sub>2</sub>/Ar. The temperature was then lowered to 538 °C and the methane conversion eventually reached the indicated steady-state value of 73%. Several successive temperature ramps (up and down) were carried out to ensure that the catalyst was in the fully oxidized state. The oxidized catalyst exhibited relatively high activity, with the methane conversion dropping slightly from 73% at 10% O<sub>2</sub> to 63% conversion at 0.5% O<sub>2</sub>. Decreasing the O<sub>2</sub> feed concentration to 0.2% led to a sharper conversion drop to 54%. A further decrease to 0.1%, which traversed the  $S_N = 1$  boundary (0.16% O<sub>2</sub>), led to an increase in the methane conversion to over 90%; this transition is indicated by the dotted 'transient path' line in Fig. 2b. A subsequent increase in the O<sub>2</sub> feed concentration from 0.1% to 0.15% resulted in an extinction to a low conversion branch. This was followed by an increase in the O<sub>2</sub> concentration back to the lean regime (0.5%). However, the catalyst remained in a low conversion state. We return to the stability of this low conversion branch later.

Methane conversions exceeding 90% were observed in the rich regime, but these high conversion levels were mostly of a transient nature and were manifested as multiple branches of states. By "transient" we imply time-dependent or non-steady-state. In a typical experiment, methane oxidation was initiated from ambient temperature to the final temperature of interest, and then successive increases and decreases in the O<sub>2</sub> feed concentration were carried out while holding the temperature constant. Fig. 3 shows the results at an O<sub>2</sub> feed concentration of 0.05% (rich regime) and feed temperature of 538 °C, which was achieved with a 5 °C min<sup>-1</sup> ramp. One hour after the ramp was stopped, the temperature settled at 538 °C while the CH<sub>4</sub> conversion settled at  $\sim 80\%$ . The O<sub>2</sub> feed concentration was then increased to 0.17%, causing an extinction, then decreased to 0.05% to achieve ignition and re-establish the high conversion state, shown as the 84% conversion value at 0.05% O<sub>2</sub> in Fig. 3. The O<sub>2</sub> feed concentration was then increased in 0.01% increments to 0.15% which traced out the highest methane conversion branch shown in Fig. 3. The peak methane conversion of 94% was observed at 0.11% O<sub>2</sub>. It is noted that this highest conversion branch was of a transient nature; i.e., without a temporary increase in the O<sub>2</sub> concentration to the lean regime the methane conversion gradually decreased over time. We return to this point later. The low methane conversion branch was encountered when the O<sub>2</sub> feed concentration was increased to 0.15%, which resulted in extinction from the high conversion branch to a low conversion branch. A subsequent gradual decrease in the O<sub>2</sub> concentration from 0.15% to 0.05%, while the catalyst was in the low conversion state, resulted in an ignition with the methane conversion increasing to 84%. Both the extinction and ignitions were reproducible in terms of the O<sub>2</sub> feed concentrations

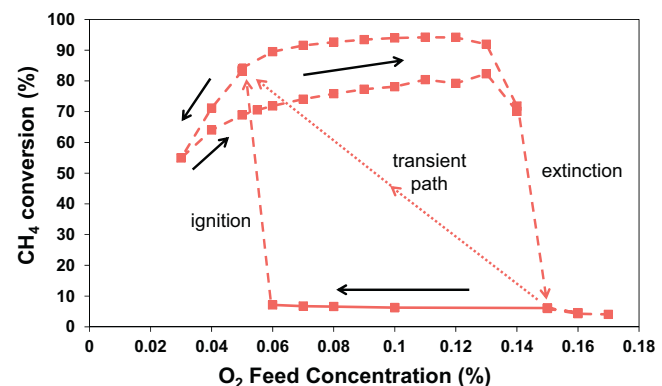


Fig. 3. Methane conversion dependence on O<sub>2</sub> feed concentration. The arrows show the directions of increases and decreases in the O<sub>2</sub> feed concentration. ( $T_f = 538^\circ\text{C}$ , 800 ppm CH<sub>4</sub>, GHSV = 60,000 h<sup>-1</sup>).

of 0.15% and 0.05%, respectively. The low conversion steady-state, at least for  $O_2$  concentrations less than ~0.2%, appeared to be stable.

The hysteresis loop existing in the rich regime was characterized by more than one high conversion branch which spanned  $O_2$  feed concentrations approaching ~0% to a concentration near the stoichiometric limit ( $S_N = 1$ : 0.16%  $O_2$ ). More than one high conversion branch was obtained depending on the starting point and history. It is interesting to note that some of the  $CH_4$  conversion points obtained at a low  $O_2$  feed concentration (<0.2%  $O_2$ ) exceeded the highest methane conversion in the lean regime which had  $O_2$  concentrations up to 10%. The multiple high conversion branches were obtained through various strategies of adjusting the  $O_2$  feed concentration. For example, starting in the lean regime (~0.5%), the  $O_2$  feed concentration was lowered to just below 0.05%, prompting an ignition, then lowered briefly to 0.02%, and then increased to 0.1%. These steps resulted in a methane conversion that approached the indicated 70% (Fig. 3). If the same initial sequence of steps was followed but the  $O_2$  concentration was instead increased just after ignition, the methane conversion followed a different locus of values. The lower of the two high conversion branches in Fig. 3 was obtained upon decreasing the  $O_2$  concentration after ignition from the low conversion branch. The methane conversion dropped to 71% at an  $O_2$  feed concentration of 0.04%, and to 55% as the  $O_2$  was decreased further to 0.03%. Increases in  $O_2$  feed from this point traced the lower of the high conversion branches in Fig. 3. As described earlier, the higher of the two high conversion branches was obtained by ignition from the extinguished branch. After reaching a lower conversion branch, the higher transient methane conversion branch in the rich regime could be recovered by briefly exposing the catalyst to a stoichiometric excess of  $O_2$  then lowering the  $O_2$  to 0.05% to achieve ignition.

Extensive operation of the reaction in the high conversion rich regime led to the conclusion that there was only one truly stable high methane conversion branch. Fig. 4 depicts the transient trend of the higher conversion states of gradual approach to a lower bound high conversion branch. The transient approach to the stable branch was rather slow, taking on the order of several hours. As we expand upon later, we speculate that the long transients are symptomatic of a depleting supply of oxygen from the bulk of the  $PdO$  phase of the bimetallic crystallites. The transient approach to steady-state was faster at lower  $O_2$  feed concentrations. We exploited this feature to systematically converge on the ultimate steady-state conversion branch through repeated  $O_2$  feed decreases and increases.

The response of the catalyst at  $O_2$  feed concentrations beyond the rich regime exhibited complex behavior. Instead of decreasing the  $O_2$  feed concentration after extinction at 0.15% in the

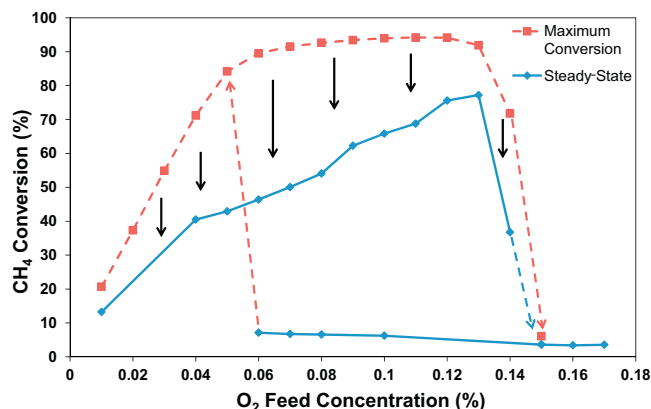


Fig. 4. Maximum conversion after light-off (red squares, ■) will eventually decrease to steady-state (blue diamonds, ♦) ( $T_f = 538^\circ C$ , 800 ppm  $CH_4$ , GHSV = 60,000  $h^{-1}$ ).

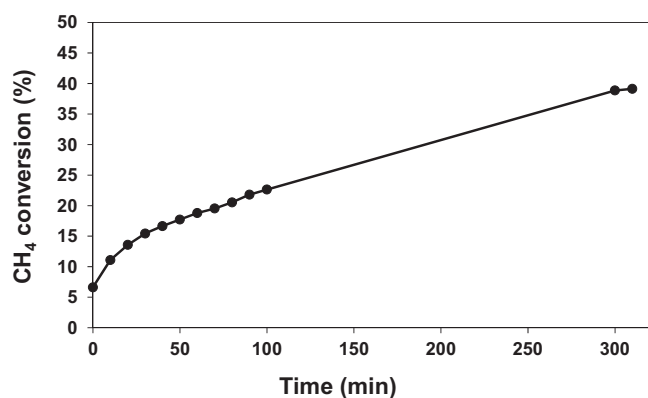


Fig. 5. Transient increase in the methane conversion from low conversion branch under lean conditions ( $T_f = 538^\circ C$ , 800 ppm  $CH_4$ , 10%  $O_2$ , GHSV = 60,000  $h^{-1}$ ).

538 °C experiment the  $O_2$  concentration was increased into the lean regime (>0.16%). This resulted in the methane conversion remaining quite low (<5%), resulting in a low conversion branch that spanned  $O_2$  concentrations from 0.06% up to the highest value of 10% (Fig. 2a). However, we found upon further investigation that there was evidence for the low conversion branch becoming unstable in the lean regime. Fig. 5 shows typical data of a slow increase in the methane conversion when the  $O_2$  feed concentration was held at 10%. We did not pinpoint the exact  $O_2$  feed concentration above which this low branch became unstable, but it was within the lean regime.

Selectivities of the carbon-containing oxidation products ( $S_{CO}$ ,  $S_{CO_2}$ ) and the  $O_2$  conversion were quantified in the rich regime. Fig. 6 shows the  $S_{CO}$  and  $S_{CO_2}$  selectivities (defined as the percentage of  $CH_4$  converted to either  $CO$  or  $CO_2$ , respectively) along two of the upper branches. Note that no other C-containing species were detected, so necessarily  $S_{CO} + S_{CO_2} = 100$ . In addition, the  $O_2$  conversion was 100% (complete) for all of the points along the upper branches (in the rich regime) reported in the earlier figures and in Fig. 6. This was confirmed by the lack of any measurable  $O_2$  peaks in the mass spectrometer. The data show that  $CO$  selectivity decreases with increased  $O_2$  feed concentration, with a corresponding increase in  $CO_2$  selectivity. In addition, at a fixed  $O_2$  feed concentration,  $S_{CO}$  increases with increasing methane conversion. This latter observation is consistent with the fact that a higher methane conversion infers a higher ratio of the C consumed to O consumed. Finally, along the low methane conversion branch  $CO_2$  was the only C-containing product; i.e.  $S_{CO_2} = 100\%$ .

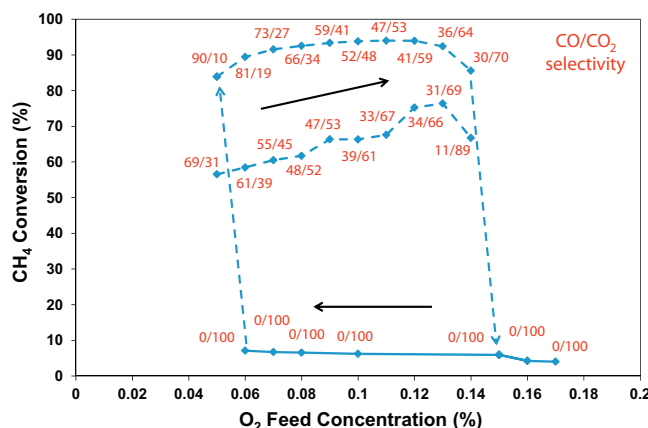
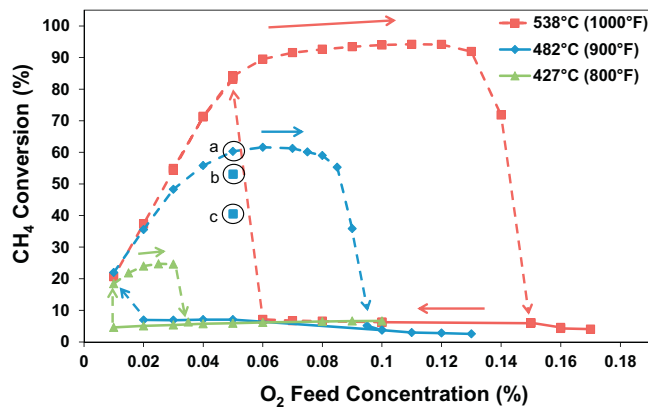


Fig. 6. Carbon selectivity for methane conversion to  $CO$  and  $CO_2$  ( $T_f = 538^\circ C$ , 800 ppm  $CH_4$ , GHSV = 60,000  $h^{-1}$ ).



**Fig. 7.** Methane conversion dependence on O<sub>2</sub> feed concentration at 538, 482, and 427 °C (800 ppm CH<sub>4</sub>, GHSV = 60,000 h<sup>-1</sup>). Note: The spatial concentration profiles for data points a, b, and c are shown in Fig. 10.

Experiments carried out with lower feed temperatures revealed a similar clockwise hysteresis behavior in the rich regime. Fig. 7 shows the results for three different temperatures spanning 427–538 °C. The size of the hysteresis loops decreased with decreasing temperature, as determined by the magnitude of the maximum methane conversion and the range of O<sub>2</sub> feed concentrations over which multiple states were observed. At higher catalyst temperatures there was an increase in the maximum conversion and a broadening of the range of O<sub>2</sub> concentration over which a high methane conversion could be sustained. While the qualitative behavior is similar, the methane conversion decreased notably with decreasing feed temperature. For example, the maximum methane conversion was 25% at 0.025% O<sub>2</sub> for 427 °C and 62% at 0.06% O<sub>2</sub> for 482 °C, in comparison to 94% obtained at 0.11% for 538 °C.

TEM combined with EDS provide important insight into the nature of the PtPd particles. Fig. 8 displays a representative micrograph showing metal nanoparticles appearing as dark dots in the grayish transparent particles of the alumina support. Some of the alumina particles have an elongated shape. Metallic particle sizes range from 10 to 40 nm, with a mean size of ~15–20 nm. The figure includes arrows with black, gray, and white shades; these respectively correspond to particles having compositions corresponding to Pt-rich (Pt/Pd > 1.5), PtPd (Pt/Pd = 0.67 to 1.50), and

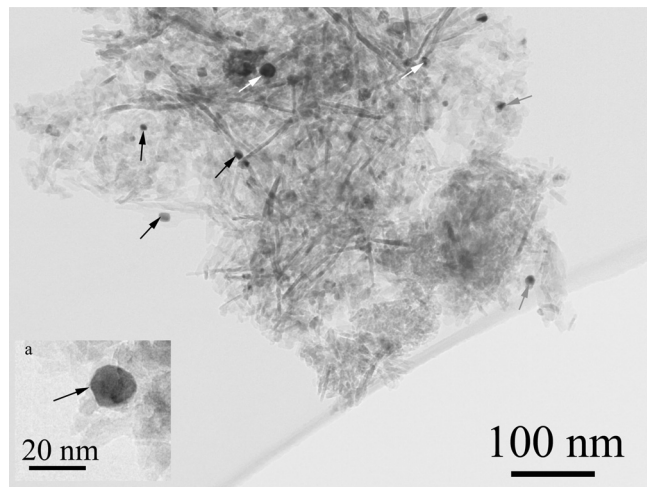


**Fig. 8.** Conventional bright field TEM image of the Pt–Pd nanoparticles embedded into alumina. One nanoparticle is shown at the higher magnification in the insert a. Shaded arrows indicate particles with composition Pt-rich (gray), Pd-rich (white), or equimolar (black).

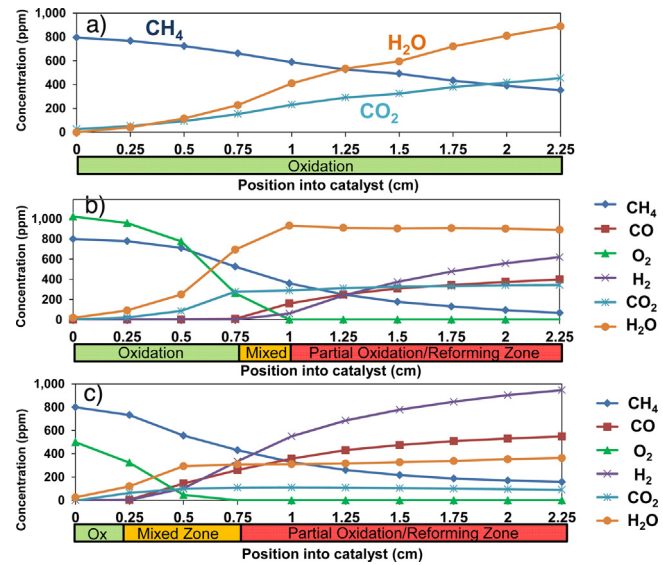


**Fig. 9.** Spatially resolved concentration profiles during methane oxidation in (a) the lean regime (10% O<sub>2</sub>), and rich regime (b: 0.1% O<sub>2</sub>; c: 0.05% O<sub>2</sub>). All other conditions were fixed (T<sub>f</sub> = 538 °C, 800 ppm CH<sub>4</sub>, GHSV = 60,000 h<sup>-1</sup>).

Pd-rich (Pt/Pd < 0.67). The size and morphology of the nanoparticles do not appear to depend on the composition. No monometallic Pt or Pd particles were identified; however, the bimetallic compositions did cover a wide range.

A total of 55 particles were analyzed from three separate locations on the grid, with each location yielding a different average Pt/Pd molar ratio. The first location contained many Pd-rich particles, with 8 out of 25 analyzed containing >60% Pd, with the maximum being an 83% Pd particle. The average composition of the first location was 52:48 Pt:Pd, which is very near the catalyst manufacturer's stated ~50:50 composition. Two additional locations analyzed were Pt-rich, with average compositions of 78:21 Pt:Pd and 64:36 Pt:Pd. The overall average atomic composition of the particles analyzed from the three locations came to 64:36 Pt:Pd. This make-up differs from the manufacturer's stated composition; however, it is likely that a larger sampling would lead to an average closer to the expected Pt/Pd = 1 ratio.

Spatially resolved concentration measurements provide detailed insight about the evolution of reaction pathways within the reactor. This is of particular interest in the rich regime in which products from both partial and complete oxidation of methane were observed. Fig. 9 shows concentration profile data for three different O<sub>2</sub> feed concentrations spanning lean (Fig. 9a: 10% O<sub>2</sub>) and rich feeds (Fig. 9b: 0.1%; Fig. 9c: 0.05%) for a feed temperature fixed at 538 °C. The spatial position indicates the axial distance from the front face of the monolith; i.e. the front and rear faces of the monolith are at the 0.0 and 2.54 cm positions, respectively.

With a feed containing excess O<sub>2</sub> only complete oxidation occurs. (This is indicated by the green bar denoting complete oxidation.) Fig. 9a. displays the concentration profiles through the catalyst under the conditions that produced the data point at 10% O<sub>2</sub> and ~70% CH<sub>4</sub> conversion in Fig. 2. The CH<sub>4</sub> concentration decreases monotonically from its feed value of 800 ppm while expectedly the CO<sub>2</sub> increases, such that C<sub>CH<sub>4</sub></sub> + C<sub>CO<sub>2</sub></sub> ≈ 800 ppm. The H<sub>2</sub>O:CO<sub>2</sub> = 2 stoichiometry is evident from the H<sub>2</sub>O profile beyond the 0.75 cm mark. At the 2.25 cm mark the SpaciMS measurement gave a CH<sub>4</sub> concentration of 353 ppm, which corresponds to a CH<sub>4</sub> conversion of 56%. Simultaneous measurement of the effluent CH<sub>4</sub> concentration by the FTIR was 258 ppm (68% conversion). The decrease in CH<sub>4</sub> concentration between measurement points ( $\Delta z = 0.25$  cm) is ~50 ppm (an incremental 6.3% in methane

conversion). Extrapolating this to what might be measured by the SpaciMS at the outlet (2.54 cm mark) gives 295 ppm (63% conversion), which is comparable to the aforementioned 68%, indicating good agreement between the FTIR and SpaciMS measurements. The FTIR essentially measures the cup-mixing average outlet concentration, while the SpaciMS obviously only measures the composition in one channel. Differences between single channel and overall conversions may be explained in part by potential variations between channels in temperature, catalyst loading, washcoat thickness, and dilution effects, among other factors.

The spatially resolved concentration measurements uncover more complex features under rich conditions. Figs. 9b and 9c show the reacting species concentrations for  $O_2$  feed concentrations of 0.1% (1000 ppm) and 0.05% (500 ppm), respectively. These profiles were obtained when the catalyst was oxidizing methane near the maximum conversion, depicted as the 0.1%  $O_2$ , ~90% conversion and at 0.05%  $O_2$ , ~80% conversion in Fig. 2. Both profiles display similar features. In the front section of the reactor mainly complete oxidation of  $CH_4$  occurs as evidenced by the co-production of  $H_2O$  and  $CO_2$  in a ratio slightly exceeding 2; notable is the absence of  $H_2$  and  $CO$ . Moving further down the channel, the  $CH_4$  and  $O_2$  concentrations decrease more sharply with  $O_2$  vanishing completely at the 1 cm mark for the 0.1%  $O_2$  feed and at the 0.75 cm mark for 0.05%  $O_2$  feed. Just upstream of the  $O_2$  depletion point for the 0.05%  $O_2$  feed both  $H_2$  and  $CO$  are detected, albeit in rather small concentrations. Beyond the  $O_2$  depletion point, the  $H_2$  concentration in particular increases sharply. The appearance of  $CO$  and  $H_2$  is evidence for a combination of methane steam reforming, methane partial oxidation, and WGS reactions. The zone between the front total oxidation zone (green) and the back reforming zone (red) is a transition zone wherein all of the chemistries may be occurring. We address the mechanism in more detail in the Discussion section.

Figs. 10a–c show the concentration profiles for a lower feed temperature ( $T_f = 482^\circ C$ ) and fixed  $O_2$  and  $CH_4$  feed concentrations of 0.05% and 800 ppm, respectively. The profiles were obtained along three different high conversion branches. The highest conversion branch in Fig. 10a was obtained shortly after ignition from the lowest steady-state of the quenched catalyst, which had been exposed to an excess  $O_2$  concentration. A complete oxidation zone is clearly seen in the 0.75 cm upstream section and a rather wide transition zone between 0.75 and 1.25 cm wherein complete oxidation to  $CO_2 + H_2O$  and partial oxidation/reforming to  $CO + H_2$  occur simultaneously. A partial oxidation/reforming zone is observed in the downstream “anaerobic” section beyond the  $O_2$  depletion point. Note while the gas phase  $O_2$  has been depleted, a supply of oxygen from the catalyst enables continued oxidation. We return to this point later. The  $CO$  and  $H_2$  continue to moderately increase while  $CH_4$  continues to moderately decrease, while the  $CO_2$  profile is flat. With time on-stream there is a notable decline in the  $CH_4$  conversion and a corresponding qualitative change in the spatial profile (Figs. 10b and 10c). Collectively, these trends suggest an apparent transient decline in the integral methane conversion rate. While the complete oxidation of methane to  $CO_2$  is sustained, the partial oxidation activity to  $CO$  drops off, affecting the selectivity ratio. With longer time on-stream, the activity continues to fall, seen in Fig. 10c, such that negligible  $CH_4$  reacts after the first 1 cm. There appear to be two main distinguishing features of these lower temperature data compared to the higher temperature data shown in Fig. 9. The first feature is the more pronounced transition region wherein both complete and partial oxidation occur; i.e. section in which  $H_2$  and  $O_2$  are both nonzero. The second feature is the slower chemistry occurring in the anaerobic section. In fact, the lowest methane conversion branch (Fig. 10c) shows virtually no methane or  $CO$  conversion beyond the  $O_2$  depletion point. The reforming activity appears to nearly halt, indicating that the rates of the reforming and WGS reactions are considerably slower at the

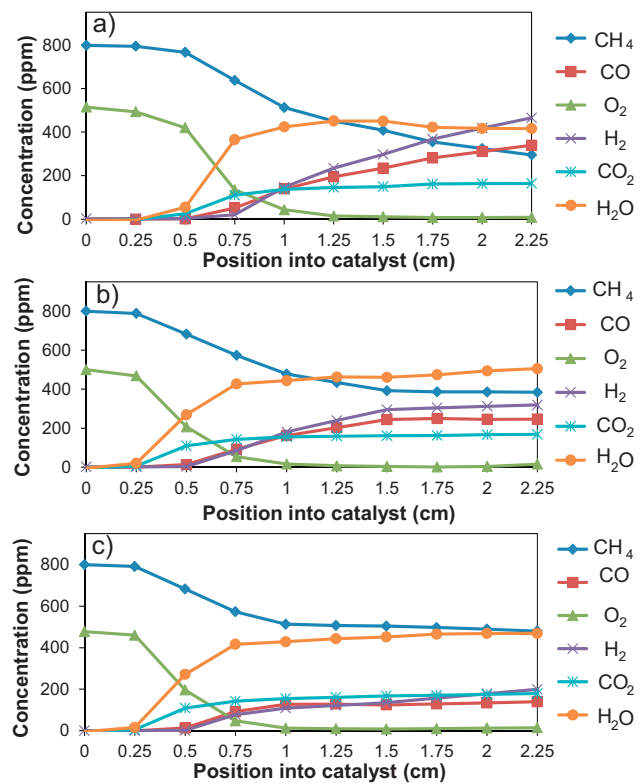


**Fig. 10.** Spatially resolved concentration profiles at three different outlet conversion points for a fixed feed  $O_2$  concentration of 0.05%. Final  $CH_4$  conversion for a) 63%, b) 52%, and c) 40% as shown in Fig. 7. All other conditions were fixed ( $T_f = 482^\circ C$ , 800 ppm  $CH_4$ , GHSV = 60,000  $h^{-1}$ ).

lower temperature. The data also display a slight shift in the reaction front toward the inlet, with one possible explanation being the formation of a small amount of more active  $PdO$  near the catalyst inlet where gaseous oxygen is present.

The relative reactivities of  $CO$  and  $CH_4$  were evaluated in co-feed experiments. This comparison provides useful insight about the reaction mechanism and pathway evolution. Fig. 11 shows the effluent concentrations of  $CO$  and  $CH_4$  when a feed containing 800 ppm  $CH_4$ , 4000 ppm  $CO$ , and 0.2%  $O_2$  ( $S_N = 0.56$ , a rich feed) was fed to the Pt/Pd catalyst during a  $10^\circ C \text{ min}^{-1}$  temperature ramp. The catalyst was initially exposed to  $450^\circ C$  in 10%  $O_2$  then cooled down before starting this experiment. The light-off and complete conversion of  $CO$  occurred in a temperature range ( $200$ – $275^\circ C$ ) well below the commencement of any measurable methane

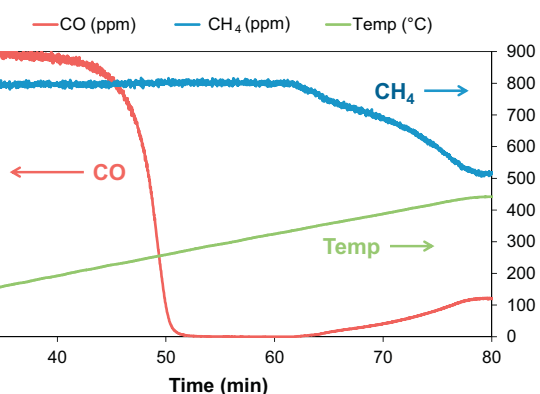


**Fig. 11.** Temperature ramp with feed containing 800 ppm  $CH_4$ , 4000 ppm  $CO$ , and 0.2%  $O_2$  (GHSV = 60,000  $h^{-1}$ ).

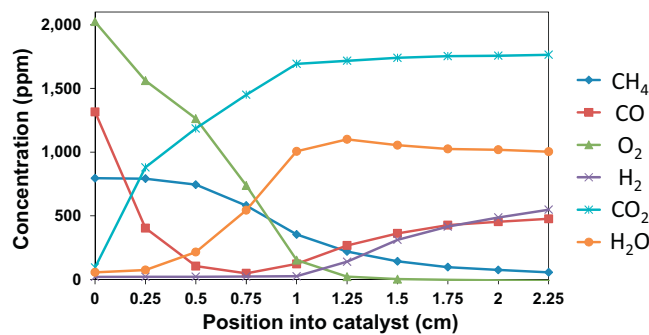


**Fig. 12.** Spatially resolved concentration measurements at 538 °C with 1400 ppm CO and 0.02% O<sub>2</sub> (GHSV = 60,000 h<sup>-1</sup>).

conversion. The complete conversion of CO should consume all of the O<sub>2</sub> since the feed ratio CO/O<sub>2</sub> = 2 is equal to the stoichiometric requirement. That methane reacts and even produces CO at higher temperature (~350 °C) could indicate that methane is competing with CO for O<sub>2</sub>. But without spatially resolved data this is not conclusive. On the other hand, given the reactivity of CO at the lower temperature and SpaciMS measurements, its re-appearance at high temperature is clearly the result of anaerobic chemistry. This was confirmed in a subsequent experiment that is described next.

Utilizing the intra-channel concentration measurements enables the reaction progression to be tracked during a co-feed of CH<sub>4</sub>, CO, and O<sub>2</sub>. Fig. 12 shows the results of an experiment in which the feed gas temperature was held at 538 °C and the feed concentrations were 800 ppm CH<sub>4</sub>, 1400 ppm CO, and 0.2% O<sub>2</sub>. The spatial profiles reveal that CO reacts first, consuming O<sub>2</sub> and generating CO<sub>2</sub>. CH<sub>4</sub> does not begin to react appreciably until the CO concentration is less than ~100 ppm. This occurs at rather low levels of gas phase O<sub>2</sub> (~700 ppm). Note that the O<sub>2</sub> feed concentration (0.2%) is above the value that led to methane conversion extinction (0.15%, Fig. 3), but the co-feed of CO enables the methane conversion light-off at higher O<sub>2</sub> feed concentration. The CO reacts with O<sub>2</sub> to produce CO<sub>2</sub> which decreases the gas phase O<sub>2</sub> concentration to a level in which methane ignition occurs. Continuing downstream where O<sub>2</sub> levels are further depleted, the partial oxidation and reforming reactions commence, generating H<sub>2</sub> and CO. At the point of O<sub>2</sub> depletion, partial oxidation/reforming and WGS chemistries take over. The intra-channel generation of CO essentially decreases the overall CO conversion when comparing the feed and effluent concentrations.

#### 4. Discussion

The experiments revealed several notable features in the dependence of the methane conversion on O<sub>2</sub> concentration spanning rich and lean feed compositions, represented schematically in Fig. 13; these are:

**Feature A:** Clockwise hysteresis loop comprising low and high steady-state conversion branches over a range of  $p_{\text{O}_2}/p_{\text{CH}_4}$  in the rich regime bounded below (above) by ignition (extinction) points;

**Feature B:** Existence of multiple transient high CH<sub>4</sub> conversion branches and single steady-state high CH<sub>4</sub> conversion branch in the rich regime;

**Feature C:** Metastable low CH<sub>4</sub> conversion branch in the lean regime;

**Feature D:** Nearly flat high CH<sub>4</sub> conversion branch in the lean regime.

Oh et al. [15] reported a sharp transition at the stoichiometric point (part of Feature A) and a high methane conversion in the lean regime (Feature D) during methane oxidation on Pd/Al<sub>2</sub>O<sub>3</sub> at high temperature. Interpretation of the steady-state, transient,

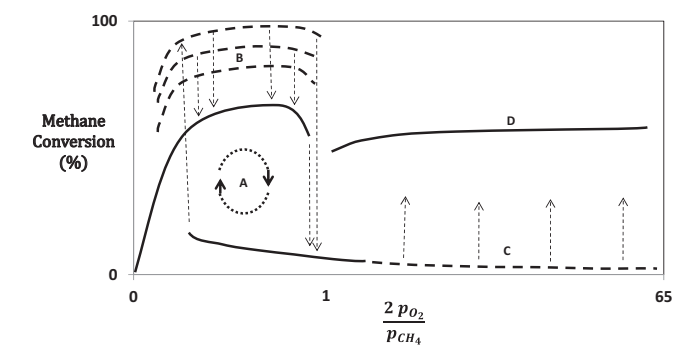
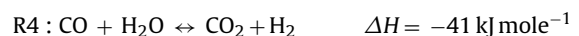
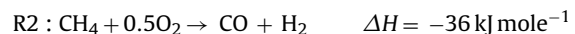
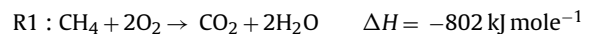


**Fig. 13.** Schematic of the methane conversion dependence on O<sub>2</sub> feed concentration at elevated temperature.

and spatio-temporal features of methane oxidation on the Pt/Pd monolith catalyst should account for the literature-established differences in the catalytic activities of Pt and Pd. The TEM+EDS measurements indicated the presence of Pt-rich, Pd-rich, and PtPd (with Pt/Pd ~ 1) crystallites. We therefore interpret the main features based on the established understanding of the underlying catalytic chemistry and kinetics of Pt, Pd, and PdO. Our analysis is aided by the detailed insight afforded by the spatially resolved data.

The clockwise hysteresis loop (Feature A, Fig. 13) reveals the existence of at least two distinct rate controlling regimes during oxygen-limited methane oxidation on Pt/Pd. Under reducing conditions there is a concomitant formation of metallic Pt, Pd, and/or PtPd alloy phases. As indicated by the formation of H<sub>2</sub> and CO, several overall reactions occur along the high conversion branch (Figs. 9, 10 and 12). The spatially resolved data indicate the complete consumption of O<sub>2</sub>, which defines aerobic and anaerobic sections in the reactor (Fig. 9). In the aerobic section both complete and partial oxidation of methane occur, while methane steam reforming and direct partial oxidation occur in the anaerobic section, and the ubiquitous WGS reaction occurs throughout:



We expand on the occurrence of multiple reactions within the monolith in more detail below.

The sharp fall-off in the conversion that occurs at high temperature near the  $S_N \sim 1$  stoichiometric point indicates inhibition of methane activation by oxygen. As mentioned, Oh et al. [15] reported in an earlier study a similar fall-off in conversion during methane oxidation on Pd/Al<sub>2</sub>O<sub>3</sub> at 550 °C. Oxygen inhibition is known to occur on both Pt and Pd. Chin et al. [29] reported a single-valued, nonmonotonic rate dependence on O<sub>2</sub>/CH<sub>4</sub> for methane oxidation on Pt/Al<sub>2</sub>O<sub>3</sub> at 600 °C. For O<sub>2</sub>/CH<sub>4</sub> < 0.08 the investigators showed that the rate is independent of excess methane and proportional to O<sub>2</sub> pressure; they further noted that CO was detected under O<sub>2</sub>-starved conditions and that the CO/CO<sub>2</sub> ratio is dictated by the WGS equilibrium. For O<sub>2</sub>/CH<sub>4</sub> > 0.08 the rate was shown to be second-order in methane and -1-order with respect to O<sub>2</sub>. The negative-order dependence on O<sub>2</sub> partial pressure was attributed to site blocking by chemisorbed oxygen adatoms. In a similar study on Pd/Al<sub>2</sub>O<sub>3</sub>, Chin and Iglesia [24] reported a more gradual decline in the oxidation rate with O<sub>2</sub> partial pressure. The methane conversion (Fig. 2) shows a rather broad range of O<sub>2</sub> concentrations in

which a high methane conversion exists. The broad range may indicate the contribution of both Pt and Pd metal sites on the alloyed particles of varying compositions.

The overlap of the high conversion, complete O<sub>2</sub> consumption state and the oxygen-inhibited, low conversion state, i.e. isothermal steady-state multiplicity, is likely a consequence of strongly nonlinear kinetics. Isothermal multiplicity has been reported for simpler reaction systems such as Pt-catalyzed CO oxidation, which has been attributed to the intrinsic kinetics or to coupling of the kinetics with transport; e.g. see Harold and Garske [65,66]. Isothermal rate multiplicity in which more than one steady-state rate exists at a given feed condition is typically a result of two or more controlling processes spanning a range of conditions. For example, the intrinsic rate of Pt-catalyzed CO oxidation is limited by CO adsorption at low CO/O<sub>2</sub> and by O<sub>2</sub> adsorption at high CO/O<sub>2</sub>. In some reports the two regimes overlap in the form of a clockwise hysteresis loop [66,67]. Eigenberger [67] showed for several generic reaction systems how the intrinsic kinetics can admit multiple solutions for some parameter values. Kevrekidis et al. [68] examined cases involving nonideal adsorption/desorption processes which lead to additional nonlinearities. Harold and Garske showed for CO oxidation how the presence of external mass transport limitations can expand the multiplicity region [66] and that the extinction point locus occurs near the stoichiometric point. The methane oxidation reaction system is more complex given the occurrence of multiple reactions and at least two different types of metal sites. That said, there are clearly two regimes; a high conversion regime in which O<sub>2</sub> is depleted within the monolith and a low conversion regime in which the rate is inhibited by O<sub>2</sub>. This is the essential ingredient for multiple states to exist. We conjecture that the overlap or steady-state multiplicity may be the result of contributions from Pd-rich and Pt-rich sites. That is, Pd may sustain the high conversion state at higher O<sub>2</sub> concentrations because the inhibition is not as dramatic as on Pt, whereas the Pt may sustain the low conversion state at lower O<sub>2</sub> concentrations because of its more intense inhibition features.

The existence of multiple transient high conversion branches in the rich regime (Feature B, Fig. 13) is attributed to the redox behavior of the Pd-rich crystallites on the bimetallic catalyst. The measured methane conversions exceeding the lower bound, stable steady-state branch (Fig. 4) are transient values that likely correspond to different extents of oxidation of the Pd catalyst. The conditions with which the Pd/Pt catalyst was initially exposed, a temperature of 550 °C and excess O<sub>2</sub>, lead to a fraction of the Pd phase of the alloyed crystallites existing in oxidized form; i.e. PdO [7]. On the other hand, since PtO<sub>2</sub> is unstable at these elevated temperatures, Pt is present in metallic form [4,69–71]. The extent of Pd oxidation depends on the exposure time, temperature, and gas phase O<sub>2</sub> concentration. The methane oxidation experiments involved a series of O<sub>2</sub> feed concentration increases and decreases that commenced at different initial conditions – or initial fractions of PdO. This resulted in what appeared to be an arbitrary number of high conversion branches within the rich regime (Fig. 3). For example, if the experiments started with a feed composition well into the lean regime ( $S_N \gg 1$ ), a subsequent decrease in the feed composition to a  $S_N$  value less than 1 resulted in methane conversion substantially higher than the eventual steady-state value. Since complete O<sub>2</sub> conversion is achieved for all of the branches including the (stable) steady-state branch, the CO/CO<sub>2</sub> selectivity ratio varies from branch to branch for a fixed O<sub>2</sub> feed concentration. With time-on-stream, the methane conversion slowly decreases while the CO/CO<sub>2</sub> selectivity ratio also decreases until the system reaches a steady-state. These observations point to the effect of a transient supply of oxygen from PdO, which is eventually completely consumed in the rich regime. Ultimately a steady-state level of Pd/PdO is established at a given O<sub>2</sub> feed concentration in the front section of the catalyst.

This steady-state corresponds to the lowest of the high conversion branches.

The transient behavior of the catalyst depends on its initial state and the path taken from that state. Consider that the bimetallic catalyst is initially in the high methane conversion state but still within the rich regime ( $S_N < 1$ ). A decrease in the O<sub>2</sub> feed concentration results in the traversing of a distinct path in the methane conversion versus O<sub>2</sub> concentration plane. The decrease in O<sub>2</sub> concentration results in the Pd phase of the PtPd alloyed particles undergoing reduction which results in a higher fraction of metallic Pd. Upon a subsequent increase in the O<sub>2</sub> feed concentration, chemisorbed oxygen blocks active catalytic sites, but Pd does not quickly form the more catalytically active PdO phase. This transient response is consistent with the observed hysteresis in the decomposition of PdO to metallic palladium and re-formation of PdO, as reported by others [26,33–35]. The temperatures of thermal decomposition and re-oxidation of Pd are dependent on the gas composition (e.g. O<sub>2</sub> concentration), temperature, and Pt/Pd ratio [8]. Bell and coworkers [27,28] showed that the Pd/PdO redox features proceed via a shrinking/expanding core mechanism.

Now consider starting with the catalyst in the low conversion state having just experienced extinction. This low conversion state persists well into the  $S_N > 1$  feed composition regime. At a high enough O<sub>2</sub> feed concentration the low conversion state becomes unstable. That is, the low methane conversion branch in the lean regime (Feature C, Fig. 13) gradually shifts to higher conversion, taking several hours. For example, for a feed containing 10% O<sub>2</sub> the methane conversion increased from ~5 to ~40% in 300 min (Fig. 5). This transient is indicative of a slow modification of a relatively inactive PtPd catalyst inhibited by O adatoms (O-Pt/O-Pd) gradually transforming to a more active catalyst comprising PdO and still-poisoned Pt crystallites; i.e. O-PtPdO. This metastability of the low conversion branch in the lean regime is consistent with previous works, if one assumes that the Pd crystallites on the PtPd particles behave like their monometallic counterparts. For example, Burch and coworkers [72] measured the O<sub>2</sub> uptake on an initially reduced Pd/Al<sub>2</sub>O<sub>3</sub> catalyst exposed to a feed gas containing 9 torr O<sub>2</sub> and at 300 °C. They showed an initial rapid uptake of a single monolayer of O followed by a much slower uptake until an O/Pd ratio of ~4 at which point the methane conversion reached ~50%. Oh et al. [15] reported a low conversion branch beyond the stoichiometric point and noted “A transition from the low conversion branch in the net-oxidizing regime could not be achieved simply by varying the O<sub>2</sub> concentration in the feed.” They speculated that an observed dependence on temperature in affecting the shift from the low conversion to high conversion branch could be related to bulk Pd oxide formation. Building on this explanation, we speculate that oxygen adatoms occupy surface sites and are effective in blocking methane adsorption as the O<sub>2</sub> concentration is increased, leading to the sharp drop in the conversion just into the rich regime. Then over time the oxygen-covered Pd crystallites transform to a more active PdO phase. The rate of the transformation process apparently increases at temperatures below ~500 °C. From this point alone, more research is needed to understand the catalyst composition and structural changes that affect the observed slow transition to a higher activity. In addition, this behavior raises some interesting issues about methane conversion during the anticipated transients encountered.

The fourth feature (Feature D, Fig. 13) in the methane conversion versus O<sub>2</sub> concentration plot is the existence of a stable methane conversion branch in the lean regime. In this regime the conversion is rather insensitive to the O<sub>2</sub> concentration and was obtained either by starting the reaction at a high (>10%) or low but still lean (~0.2%) O<sub>2</sub> concentration. This branch appears to be the classical lean methane oxidation on PdO, likely on the Pd-rich nanoparticles. Many previous studies have shown the very good activity of PdO

and Pt/Pd catalysts, noting that for the latter PdO has been shown to be present as a separate phase (refer to Introduction). Moreover, the kinetics of lean methane oxidation in the 450–600 °C temperature range have been reported to be near unity order for methane and zero order for O<sub>2</sub> [28].

The SpaciMS measurements provide insight on the competing catalytic reactions. As mentioned earlier, there is evidence for complete oxidation, partial oxidation, steam reforming, and WGS chemistries. The complete oxidation of CH<sub>4</sub> is the lone overall reaction for a lean feed (reaction R1 above). Fig. 9a shows this conventional consumption of CH<sub>4</sub> and formation of CO<sub>2</sub> and H<sub>2</sub>O for a feed containing 800 ppm CH<sub>4</sub> and 10% O<sub>2</sub> ( $S_N = (2 \times 100000)/(4 \times 800 + 0) = 62.5$ ) and feed temperature of 538 °C. Complete oxidation also occurs at the front part of the reactor when the feed is overall net rich ( $S_N < 1$ ). For example, for the feed containing 800 ppm CH<sub>4</sub> and 500 ppm O<sub>2</sub> (Fig. 9c) ( $S_N = (2 \times 500)/(4 \times 800 + 0) = 0.31$ ) CO<sub>2</sub> and H<sub>2</sub>O are the only products in the front 0.25 cm section of the reactor. Evidence for partial oxidation of methane is the presence of CO and/or H<sub>2</sub> (reaction R2). These products consistently appeared in the absence of gas phase O<sub>2</sub>. For a net-reducing feed ( $S_N < 1$ ) and a sufficiently high temperature, complete conversion of gas phase O<sub>2</sub> was observed. At the point in the reactor in which O<sub>2</sub> was depleted there was an emergence and increase in the incremental production of H<sub>2</sub> in particular and CO to a lesser extent. At high temperatures there was some evidence for methane steam reforming (R3) or WGS (R4) due to a reduction in the H<sub>2</sub>O concentration along the reactor length (see Fig. 9b). The incremental production of H<sub>2</sub> and CO is not expected to be equal due to the H<sub>2</sub>:CO = 3 ratio during partial oxidation as well as potential consumption of CO in favor of H<sub>2</sub> by the WGS reaction. It is noted that the extent of methane steam reforming was not that significant at the temperatures considered in this study. At the highest temperature (538 °C) and after steady-state (stored oxygen depletion) was established, only a few percent of CH<sub>4</sub> continued to react in the back section of the reactor in the absence of O<sub>2</sub>.

The spatial profiles provide evidence for partial oxidation of methane by oxygen supplied from the catalyst. The three different methane conversion levels obtained at 482 °C correspond to different degrees of approach to steady-state (Fig. 10). The highest conversion state (Fig. 9a) was obtained shortly after the catalyst had been exposed to an increased level of O<sub>2</sub>. The methane profile clearly shows continued conversion even after depletion of gas phase O<sub>2</sub> within the reactor ( $z > 1.25$  cm). The increasing CO profile in this region suggests sustained partial oxidation in the absence of O<sub>2</sub>. In comparison, the profiles obtained after steady-state was reached (Fig. 10c) show a much less pronounced methane consumption and CO production. This would seem to rule out any significant contribution of steam reforming at this temperature. Thus, the change in methane partial oxidation/reforming activity in the back portion of the catalyst is attributed to stored (bulk) oxygen which diffuses to the PdO phase of the bimetallic catalyst surface during rich conditions. As the stored oxygen becomes depleted over time, less methane reacts. This helps to explain why in the back portion of the catalyst the SpaciMS measurements show continued reaction of CH<sub>4</sub> to produce CO and H<sub>2</sub>, even after all O<sub>2</sub> was consumed while not showing the corresponding consumption of H<sub>2</sub>O. By extinguishing the reaction with excess oxygen, the lattice oxygen is replenished and the maximum conversion may be restored upon light-off.

Further evidence for the enhancement of CH<sub>4</sub> conversion through reaction with stored oxygen can be gleaned from the oxygen material balance. In the experiment in which a constant O<sub>2</sub> concentration of 500 ppm (total of 1000 ppm oxygen atoms) was supplied three spatial profiles were obtained at different times on stream (Fig. 10). With increasing time-on-stream the total oxygen contained in the gaseous products decreased as

evidenced by analysis of the CO, CO<sub>2</sub>, and H<sub>2</sub>O concentrations at the 2.25 cm position in the reactor. Shortly after oxygen replenishment (Fig. 10a), the product stream contained 1083 ppm O (416 ppm H<sub>2</sub>O + 339 ppm CO + 2 × 164 ppm CO<sub>2</sub>), which is a level well above the feed value of 1000 ppm O. After some time (Fig. 10c) the total oxygen contained in the products at the 2.25 cm position was 967 ppm O (469 ppm H<sub>2</sub>O + 140 ppm CO + 2 × 179 ppm CO<sub>2</sub>). Moreover, considerably less CO was formed, a more likely product from reaction between CH<sub>4</sub> and oxygen supplied from PdO. This analysis reinforces the existence of the direct partial oxidation of CH<sub>4</sub> by stored oxygen occurring in the back portion of the catalyst.

The spatial concentration profiles obtained with the co-feed of CO and CH<sub>4</sub> (Fig. 12) help to decipher the methane oxidation mechanism. The conversion of 1400 ppm of CO is nearly complete in the front 0.75 cm section, whereas the conversion of 800 ppm of CH<sub>4</sub> does not exceed 90% until the point of O<sub>2</sub> depletion at the 1.25 cm mark. The oxidation of CO in the front part of the catalyst serves to reduce the gas phase O<sub>2</sub> concentration enabling the light-off of methane oxidation. That the CO concentration does not completely vanish suggests CO and CH<sub>4</sub> oxidations have comparable rates at higher temperature. Clearly, the temperature ramp experiment (Fig. 11) shows that CO oxidation is much faster than methane oxidation at lower temperature.

## 5. Conclusions

An experimental study of methane oxidation by Pt/Pd/Al<sub>2</sub>O<sub>3</sub> washcoated monolith was carried out at oxygen feed concentrations spanning fuel lean to fuel rich. The effects of temperature and feed conditions on methane conversion and existence of axial zones in the catalyst have been systematically explored. A plot of the CH<sub>4</sub> conversion versus O<sub>2</sub>/CH<sub>4</sub> feed ratio demonstrates features of methane oxidation that are both complex and interesting. The plot shows a clockwise hysteresis loop consisting of two stable steady-states of methane conversion. The high steady-state conversion branch is eclipsed by multiple higher methane conversion branches that are transient in nature. Within the rich regime, the methane conversion is to complete (CO<sub>2</sub>, H<sub>2</sub>O) and partial (CO, H<sub>2</sub>) oxidation products with O<sub>2</sub> serving as the limiting reactant. The methane consumption observed under lean conditions is insensitive to the oxygen concentration and is classical lean methane oxidation on PdO.

An attempt is made to conjecture on the root causes of the various features of the conversion dependence on O<sub>2</sub> concentration, noting that the catalyst consists of a mixture of Pt and Pd. TEM-EDS results reveal a wide range of compositions for the PtPd alloyed particles, suggesting that the Pt, Pd, and PdO all contribute to the catalyst performance. We utilize conversion and selectivity measurements together with literature information on the behavior of Pt, Pd, and Pt/Pd catalysts during methane oxidation. The broad range of O<sub>2</sub> feed concentrations over which isothermal multiplicity occurs is likely the result of the nonlinear coupling between oxygen adsorption inhibition, PdO formation and methane conversion. The formation of PdO appears responsible for the transient supra-steady-state conversion values that were observed when transitioning from lean to rich conditions. Finally, the slow increase in conversion that occurs in the lean regime is attributed to the modification of inactive metallic Pd crystallites into active PdO with Pt still-poisoned by oxygen.

Spatially resolved intrachannel concentration measurements show an intriguing interplay between multiple chemical reactions and their spatial evolution. The measurements show the existence of different zones based on the availability of oxygen in the gas phase or on the catalyst. The complete oxidation of methane occurs under both lean and rich conditions. During operation in the

rich regime, a front oxidative zone and downstream partial oxidation/reforming zone co-exist. A middle mixed transition zone was also detected in which production of CO and H<sub>2</sub> occurs prior to complete consumption of the gas phase O<sub>2</sub>. The partial oxidation of CH<sub>4</sub> during rich phase leads to our speculation that lattice oxygen diffuses to the catalyst surface thereby continuing the production of CO and H<sub>2</sub> + H<sub>2</sub>O even after all of the available gas phase oxygen has been consumed without any corresponding consumption of H<sub>2</sub>O. Measurements taken during different high conversion states in the rich regime corroborate the existence of the direct partial oxidation of CH<sub>4</sub> by stored oxygen that takes place in the rear section of the catalyst, as well as the subsequent decline in conversion and shift in selectivity as stored oxygen is depleted. Spatial concentration profiles obtained during a co-feed of CO and CH<sub>4</sub> reveal the fast oxidation of CO in the front portion of the catalyst, which reduces the gas phase O<sub>2</sub> concentration downstream and enabled the light-off of methane oxidation.

The findings from this study have two notable implications to the practice of methane emission control. First, the hysteresis and slow transients will have a definite impact on the emission control during the inherently transient vehicle operation, as the exhaust composition, temperature, and flow rate are all time dependent. The results show that the history of the catalyst will affect its performance, with the potential for dramatic conversion differences. This undoubtedly complicates the design of the catalytic converter and the associated control system to achieve a requisite level of emission reduction over a drive cycle and underscores the need to develop a fundamental understanding of the kinetics and to capture that understanding in a predictive model. This is the subject of ongoing research. Second, the results indicate that high methane conversion can be achieved at sufficiently high temperature and relevant space velocities on a Pt/Pd monolith catalyst. The methane conversion is more effective and facile for a lean feed due to the higher activity of PdO. On the other hand, methane conversion can be achieved for a rich feed but the catalyst is very sensitive to the O<sub>2</sub> feed concentration and the byproducts include CO and H<sub>2</sub>. While the formation of CO and H<sub>2</sub> is undesirable, they could be removed in a downstream converter using supplemental air.

## Acknowledgements

We acknowledge the support of the Texas Center for Clean Engines, Emissions and Fuels (TxCEF) at the University of Houston with partial support from the National Science Foundation (CBET grant no. 1067709). We also acknowledge BASF Catalysts (Iselin, NJ) for providing the catalysts. Finally, we acknowledge helpful discussions with Professor Bill Epling.

## References

- [1] Annual Energy Outlook 2013, U.S. Energy Information Administration, Washington, DC, 2013.
- [2] O. Boucher, P. Friedlingstein, B. Collins, K. Shine, *Environ. Res. Lett.* 4 (2009) 044007.
- [3] R.B. Anderson, K.C. Stein, J.J. Feenan, L.J.E. Hofer, *Ind. Eng. Chem.* 53 (1961) 809.
- [4] P. Gelin, M. Primet, *Appl. Catal. B Environ.* 39 (2002) 1.
- [5] J.K. Lampert, M.S. Kazi, R.J. Farrauto, *Appl. Catal. B Environ.* 14 (1997) 211.
- [6] R.F. Hicks, H. Qi, M.L. Young, R.G. Lee, *J. Catal.* 122 (1990) 295.
- [7] D. Ciuparu, M.R. Lyubovsky, E. Altman, L.D. Pfefferle, A. Datye, *Catal. Rev.* 44 (2002) 593.
- [8] P. Castellazzi, G. Groppi, P. Forzatti, *Appl. Catal. B Environ.* 95 (2010) 303.
- [9] J.G. McCarty, *Catal. Today* 26 (1995) 283.
- [10] R.F. Hicks, H. Qi, M.L. Young, R.G. Lee, *J. Catal.* 122 (1990) 280.
- [11] T.R. Baldwin, R. Burch, *Appl. Catal.* 66 (1990) 337.
- [12] T.R. Baldwin, R. Burch, *Appl. Catal.* 66 (1990) 359.
- [13] P. Briot, M. Primet, *Appl. Catal.* 68 (1991) 301.
- [14] F. Klingstedt, A.K. Neyestanaki, R. Byggningsbacka, L.-E. Lindfors, M. Lunden, M. Petersson, P. Tengstrom, T. Ollonqvist, J. Vayrynen, *Appl. Catal. A Gen.* 209 (2001) 301.
- [15] S.H. Oh, P.J. Mitchell, R.M. Siewert, *J. Catal.* 132 (1991) 287.
- [16] G. Centi, *J. Mol. Catal. A Chem.* 173 (2001) 287.
- [17] K. Narui, H. Yata, K. Furuta, A. Nishida, Y. Kohtoku, T. Matsuzaki, *Appl. Catal. A Gen.* 179 (1999) 165.
- [18] C.H. Kim, M. Schmid, S.J. Schmieg, J. Tan, W. Li, *SAE Technical Paper* 2011-01-1134 (2011).
- [19] R. Burch, P.K. Loader, *Appl. Catal. B Environ.* 5 (1994) 149.
- [20] S. Subramanian, R.J. Kudla, M.S. Chattha, *Ind. Eng. Chem. Res.* 31 (1992) 2460.
- [21] S. Subramanian, R. Kudla, M.S. Chattha, *SAE Tech. Pap.* 930223 (1993).
- [22] M. Lyubovsky, H. Karim, P. Menacherry, S. Boorse, R. LaPierre, W.C. Pfefferle, S. Roychoudhury, *Catal. Today* 83 (2003) 183.
- [23] S.H. Oh, P.J. Mitchell, *Appl. Catal. B Environ.* 5 (1994) 165.
- [24] Y.H. Chin, E. Iglesia, *J. Phys. Chem. C* 115 (2011) 17845.
- [25] W.S. Epling, G.B. Hoflund, *J. Catal.* 182 (1999) 5.
- [26] S.C. Su, J.N. Carstens, A.T. Bell, *J. Catal.* 176 (1998) 125.
- [27] J.N. Carstens, S.C. Su, A.T. Bell, *J. Catal.* 176 (1998) 136.
- [28] G. Zhu, J. Han, D.Y. Zemlyanov, F.H. Ribeiro, *J. Phys. Chem. B* 109 (2005) 2331.
- [29] Y.-H. Chin, C. Buda, M. Neurock, E. Iglesia, *J. Catal.* 283 (2011) 10.
- [30] A. Yamaguchi, E. Iglesia, *J. Catal.* 274 (2010) 52.
- [31] K. Fujimoto, F.H. Ribeiro, M. Avalos-Borja, E. Iglesia, *J. Catal.* 179 (1998) 431.
- [32] T. Zhang, Y. Xin, Z. Ren, F. Qi, C.K. Law, *Combust. Flame* 160 (2013) 149.
- [33] M.M. Wolf, H. Zhu, W.H. Green, G.S. Jackson, *Appl. Catal. A Gen.* 244 (2003) 323.
- [34] A.K. Datye, J. Bravo, T.R. Nelson, P. Atanasova, M. Lyubovsky, L. Pfefferle, *Appl. Catal. A Gen.* 198 (2000) 179.
- [35] R.J. Farrauto, J.K. Lampert, M.C. Hobson, E.M. Waterman, *Appl. Catal. B Environ.* 6 (1995) 263.
- [36] A. Amin, A. Abedi, R. Hayes, M. Votsmeier, W. Epling, *Appl. Catal. A Gen.* 478 (2014) 91.
- [37] L.D. Schmidt, M. Huff, S.S. Bharadwaj, *Chem. Eng. Sci.* 49 (1994) 3981.
- [38] S.S. Bharadwaj, L.D. Schmidt, *Fuel Process. Technol.* 42 (1995) 109.
- [39] Y. Ozawa, Y. Tochihara, A. Watanabe, M. Nagai, S. Omi, *Appl. Catal. A Gen.* 259 (2004) 1.
- [40] A. Morlang, U. Neuhausen, K.V. Klementiev, F.W. Schütze, G. Miehe, H. Fuess, E.S. Lox, *Appl. Catal. B Environ.* 60 (2005) 191.
- [41] K. Persson, A. Ersson, K. Jansson, J.L.G. Fierro, S.G. Jaras, *J. Catal.* 243 (2006) 14.
- [42] T.R. Johns, J.R. Gaudet, E.J. Peterson, J.T. Miller, E.A. Stach, C.H. Kim, M.P. Balogh, A.K. Datye, *Chem. Cat. Chem.* 5 (2013) 2636.
- [43] W.P. Partridge, J. Storey, S. Lewis, R. Smithwick, G. Devault, M. Cunningham, N. Currier, T. Yonushonis, *SAE Tech. Pap.* 2000-01-2952 (2000).
- [44] B. West, S. Huff, J. Parks, S. Lewis, J.-S. Choi, W.P. Partridge, J. Storey, *SAE Tech. Pap.* 2004-01-3023 (2004).
- [45] J.-S. Choi, W.P. Partridge, C.S. Daw, *Appl. Catal. A Gen.* 293 (2005) 24.
- [46] J.-S. Choi, W.P. Partridge, W.S. Epling, N.W. Currier, T.M. Yonushonis, *Catal. Today* 114 (2006) 102.
- [47] J.-S. Choi, W.P. Partridge, C.S. Daw, *Appl. Catal. B Environ.* 77 (2007) 145.
- [48] J.-S. Choi, W.P. Partridge, J.A. Pihl, C.S. Daw, *Catal. Today* 136 (2008) 173.
- [49] W.P. Partridge, J.-S. Choi, *Appl. Catal. B Environ.* 91 (2009) 144.
- [50] P. Forzatti, L. Lietti, N. Gabrielli, *Appl. Catal. B Environ.* 99 (2010) 145.
- [51] J.-S. Choi, W.P. Partridge, J.A. Pihl, M.-Y. Kim, P. Koci, C.S. Daw, *Catal. Today* 184 (2012) 20.
- [52] V. Easterling, Y. Ji, M. Crocker, M. Dearth, R.W. McCabe, *Appl. Catal. B Environ.* 123–124 (2012) 339.
- [53] B.C. Michael, D.N. Nare, L.D. Schmidt, *Chem. Eng. Sci.* 65 (2010) 3893.
- [54] O. Shakir, A. Yezers, N.W. Currier, W.S. Epling, *Appl. Catal. A Gen.* 365 (2009) 301.
- [55] M. Al-Harbi, D. Radtke, W.S. Epling, *Appl. Catal. B Environ.* 96 (2010) 524.
- [56] A. Russell, C. Henry, N.W. Currier, A. Yezers, W.S. Epling, *Appl. Catal. A Gen.* 397 (2011) 272.
- [57] J.-Y. Luo, M. Al-Harbi, M. Pang, W.S. Epling, *Appl. Catal. B Environ.* 106 (2011) 664.
- [58] A. Abedi, J.-Y. Luo, W.S. Epling, *Catal. Today* 207 (2013) 220.
- [59] J.-Y. Luo, H. Oh, C. Henry, W. Epling, *Appl. Catal. B Environ.* 123–124 (2012) 296.
- [60] J.-Y. Luo, X. Hou, P. Wijayakoon, S.J. Schmieg, W. Li, W.S. Epling, *Appl. Catal. B Environ.* 102 (2011) 110.
- [61] X. Hou, S.J. Schmieg, W. Li, W.S. Epling, *Catal. Today* 197 (2012) 9.
- [62] M. Hettel, C. Diehm, B. Torkashvand, O. Deutschmann, *Catal. Today* 216 (2013) 2.
- [63] A. Goguet, W.P. Partridge, F. Aiouche, C. Hardacre, K. Morgan, C. Stere, J. Sa, *Catal. Today* (2014).
- [64] M. Hettel, C. Diehm, O. Deutschmann, *Catal. Today* (2014).
- [65] M.P. Harold, M.E. Garske, *J. Catal.* 127 (1991) 524.
- [66] M.P. Harold, M.E. Garske, *J. Catal.* 127 (1991) 553.
- [67] G. Eigenberger, *Chem. Eng. Sci.* 33 (1978) 1255.
- [68] I. Kevrekidis, L.D. Schmidt, R. Aris, *Surf. Sci.* 137 (1984) 151.
- [69] R. Bradley Shumbera, H.H. Kan, J.F. Weaver, *Surf. Sci.* 601 (2007) 235.
- [70] M. Kaneda, H. Iizuka, T. Hiratsuka, N. Shinotsuka, M. Arai, *Appl. Catal. B Environ.* 90 (2009) 564.
- [71] N.M. Kinnunen, J.T. Hirvi, M. Suvanto, T.A. Pakkanen, *J. Mol. Catal. A Chem.* 356 (2012) 20.
- [72] R. Burch, F.J. Urbano, *Appl. Catal. A Gen.* 124 (1995) 121.